Yafei He, Panpan Zhang, Faxing Wang, Luxin Wang, Yuezeng Su, Fan Zhang, Xiaodong Zhuang, Xinliang Feng

Vacancy modification of Prussian-blue nano-thin films for high energy-density microsupercapacitors with ultralow RC time constant

Erstveröffentlichung in / First published in:

Nano Energy. 2019, 60, S. 8 – 16. ScienceDirect. ISSN 2211-2855.

DOI: https://doi.org/10.1016/j.nanoen.2019.03.042

Accepted Manuscript

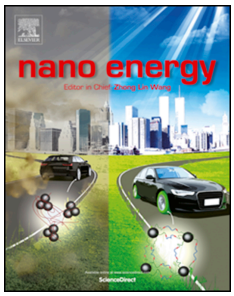

Vacancy modification of Prussian-blue nano-thin films for high energy-density micro-supercapacitors with ultralow RC time constant

Yafei He, Panpan Zhang, Faxing Wang, Luxin Wang, Yuezeng Su, Fan Zhang, Xiaodong Zhuang, Xinliang Feng

PII: S2211-2855(19)30230-7

DOI: https://doi.org/10.1016/j.nanoen.2019.03.042

Reference: NANOEN 3561

To appear in: *Nano Energy*

Received Date: 10 January 2019

Revised Date: 15 February 2019

Accepted Date: 10 March 2019

Please cite this article as: Y. He, P. Zhang, F. Wang, L. Wang, Y. Su, F. Zhang, X. Zhuang, X. Feng, Vacancy modification of Prussian-blue nano-thin films for high energy-density micro-supercapacitors with ultralow RC time constant, *Nano Energy* (2019), doi: https://doi.org/10.1016/j.nanoen.2019.03.042.

Final edited form was published in "Nano Energy". 2019, 60, S. 8 – 16. ISSN 2211-2855.
https://doi.org/10.1039/C8CC01993B

Precise vacancy modification of Prussian-blue nano-thin films for micro-supercapacitors is carried out through an efficient *in-situ* growth method

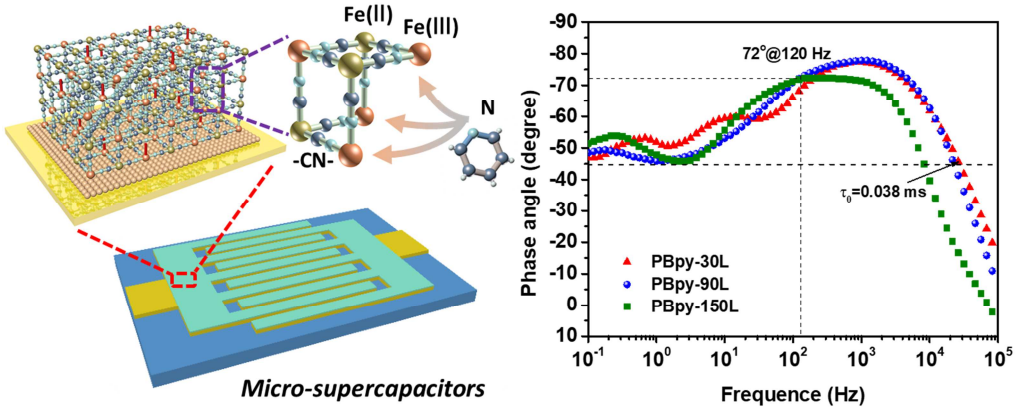

Key words:
vacancy-modification; prussian-blue; nano-thin films; micro-supercapacitors; RC time constant

Final edited form was published in "Nano Energy". 2019, 60, S. 8 – 16. ISSN 2211-2855.
https://doi.org/10.1039/C8CC01993B

Vacancy modification of Prussian-blue nano-thin films for high energy-density micro-supercapacitors with ultralow RC time constant

Yafei He[a,c,‡], Panpan Zhang[c,‡], Faxing Wang[c], Luxin Wang[a], Yuezeng Su[b,*], Fan Zhang[a,*], Xiaodong Zhuang[a], Xinliang Feng[c]

[a] *School of Chemistry and Chemical Engineering, The State Key Laboratory of Metal Matrix Composites & Shanghai Key Lab of Electrical Insulation and Thermal Ageing, Shanghai Jiao Tong University, Shanghai 200240, P. R. China*

[b] *School of Electronic Information and Electrical Engineering, Shanghai Jiao Tong University, 200240, Shanghai, P. R. China*

[c] *Center for Advancing Electronics Dresden (cfaed) & Department of Chemistry and Food Chemistry, Technische Universität Dresden, Mommsenstrasse 4, Dresden 01062, Germany*

* Corresponding authors. E-mail: fan-zhang@sjtu.edu.cn (F. Zhang), yzsu@sjtu.edu.cn (Y. Su)

‡ These authors contributed equally to this work

Abstract

In-plane micro-supercapacitors (MSCs), as promising power candidates for micro-devices, typically exhibit high power densities, large charge/discharge rates, and long cycling lifetimes. The high areal/volumetric capacitances, high energy/power densities, high rate capability, as well as flexibility are the main scientific pursue in recent years. Among diverse electrode materials for MSCs, coordination polymer frameworks are emerging due to the designable porous structure and tunable functionality. However, the unsatisfied electrochemical performance still hinders their practical applications. In this work, we demonstrate the first time an efficient *in-situ* growth approach to precisely modify the vacancy of Prussian-blue nano-thin films with pyridine by coordination reaction for high energy-density MSCs. Confirmed by the experimental results and

Final edited form was published in "Nano Energy". 2019, 60, S. 8 – 16. ISSN 2211-2855.
https://doi.org/10.1039/C8CC01993B

density functional theory calculation, the vacancy modification within Prussian-blue network improved the film-forming property, hydrophilicity, and electrochemical activity of the thin films. The resultant MSCs based on pyridine-modified Prussian-blue exhibited an ultrahigh energy density of up to 12.1 mWh cm^{-3} and an ultra-low time constant (τ_0) of 0.038 ms, which are the best values among the state-of-the-art in-plane MSCs. This work provides an attractive solution for structural engineering of promising active materials on molecule level toward high-performance micro-energy devices.

1. Introduction

In-plane micro-supercapacitors (MSCs) have attracted considerable research interests because of their high power densities, large charge/discharge rates, fast frequency responses, and superior cycling stabilities [1,2], which are promising power candidates for modern microelectronic devices, e.g. portable electronics, wearable devices and implantable devices [3-5]. The high areal/volumetric capacitances, high energy/power densities, high rate capability, as well as flexibility are the main scientific pursue for MSCs in recent years [6,7]. The thin-film fabrication technique plays a vital role to achieve high-performance in-plane MSCs. Some thin-film processing methods, involving conventional photolithography [8], laser-scribing [9-11], screen printing [12,13], and ink-jet printing [14-17], have been explored for obtaining MSCs based on various materials, such as nanocarbons [18-20], metal compounds [21-25], and conducting polymers [26-28]. Unfortunately, these fabrication methods entail relatively harsh conditions, including high-temperature treatment, high-energy laser or plasma source, and acid etching, which

Final edited form was published in "Nano Energy". 2019, 60, S. 8 – 16. ISSN 2211-2855.
https://doi.org/10.1039/C8CC01993B

greatly hinder their practical applications. Developing scalable and sustainable thin-film fabrication strategies for obtaining high-performance MSCs remains a challenge.

Recently, coordination polymer frameworks [29-31] are emerging class of electrode materials for electrochemical devices due to some excellent characters such as designable porous structures, dense redox active sites, structural diversity, and tunable functionality [32-35]. However, exploring their application for in-plane MSCs still remains in an early stage, mostly due to the lack of compatible strategy for fabricating high-active nano-thin films. We lately reported the first example of coordination polymer framework-based MSC [35], which unfortunately exhibited a relatively low energy density due to limited redox activity and imprecise control over the nanoscale thickness in a tedious synthetic procedure. Therefore, synthesizing controllable coordination polymer frameworks-based thin films with remarkable redox activity is highly desirable.

Prussian-blue (PB) and its analogs are one class of non-toxic, cost-efficient, and highly redox-active coordination polymer frameworks [36-39]. The chemical structure of ferric ferrocyanide ($Fe^{III}_4[Fe^{II}(CN)_6]_3$) for Prussian-blue typically consists of one high-spin Fe(III) central atom and one low-spin Fe(II) central atoms, which are coordinated to nitrogen and carbon atoms, respectively. It is revealed that numerous [$Fe(CN)_6$] vacancies which are always occupied by coordinated water in the PB lattice can largely suppress its electrochemical activity [40]. Some efforts have been made to reduce the number of these vacancies including using the gradual growth-approach [41], carbon black [42], and graphene-oxide [43]. However, a precise functionalization of vacancy at the molecule level remains quite scarce. Moreover, the formation of PB-derived thin film with finely tuned thickness at nanoscale level and robust mechanical stability is still far

Final edited form was published in "Nano Energy". 2019, 60, S. 8 – 16. ISSN 2211-2855.
https://doi.org/10.1039/C8CC01993B

from success, presumably suffering from the rapid crystallization as in the most cases of coordination polymers. Thus, PB has not been used as electrode materials in the fabrication of in-plane MSCs yet. With these in our mind, here we attempted to precisely modify the $[Fe(CN)_6]$ vacancies within the PB network by coordinating organic Lewis-base ligands of pyridine with Fe central atoms, primarily on the basis of the following considerations: (1) promoting an increase in the electrochemical activity of PB through ligation with strong-field pyridine units; (2) improving the thin film-forming property by addition of organic components, and (3) increasing of the mass transport by tailoring the polarity and space of network channels via organic-inorganic hybridization.

In this work, we demonstrate an efficient *in-situ* growth approach to precisely modify the vacancy of Prussian-blue nano-thin films with pyridine through coordination reaction for high energy-density MSCs. A series of pyridine-modified Prussian-blue (PBpy) thin films can be directly in-situ grown on the gold interdigital current collectors with rationally controlled nanoscale thickness. Confirmed by experimental results and density functional theory calculation, the vacancy modification within Prussian-blue network improved the film-forming property, hydrophilicity, and electrochemical activity of the thin films. The resultant PBpy-based MSCs delivered remarkable areal capacitances of up to 4.69 mF cm^{-2} and volumetric capacitances of up to 347 F cm^{-3}, with ultrahigh energy densities reaching up to 12.1 mWh cm^{-3}, outperforming most other reported MSCs. In particular, an achieved ultra-low resistance-capacitance (RC) time constant (τ_0) of 0.038 ms for PBpy-based MSC is the best value of the state-of-the-art in-plane MSCs.

Final edited form was published in "Nano Energy". 2019, 60, S. 8 – 16. ISSN 2211-2855.
https://doi.org/10.1039/C8CC01993B

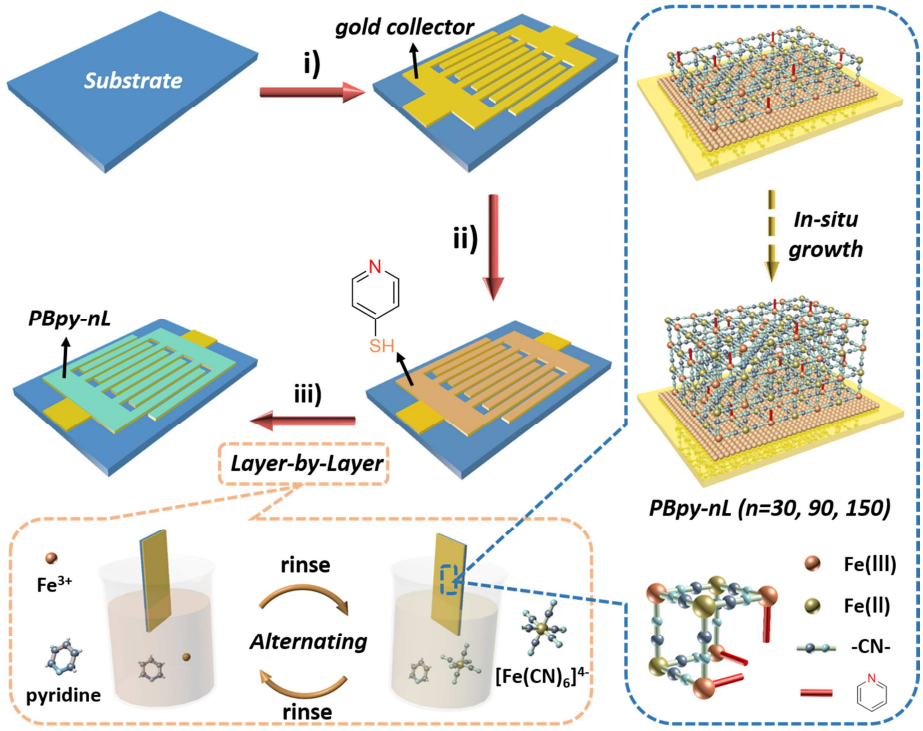

Fig. 1. Illustration of *in-situ* growth of PBpy thin films as electrode materials for MSCs, i) fabrication of gold microelectrode with interdigital pattern through thermal evaporation; ii) functionalization for the surface of the gold via 4-mercaptopyridine; iii) immersing functionalized microelectrode alternately in ethanol solution of $FeCl_3$ and pyridine, deionized water, aqueous solution of $K_4Fe(CN)_6$ and pyridine, and deionized water for 30 cycles, 90 cycles, and 150 cycles.

2. Result and discussion

A concise synthetic approach to PBpy thin films is depicted in Fig. 1. In a typical procedure, a gold microelectrode with interdigital geometry was first patterned as collector on SiO_2/silicon wafer through thermal evaporation using a lab-made mask. Then, the microelectrode was functionalized by densely grafting 4-mercaptopyridine on the surface of the gold via the coordination with mercapto groups [29]. The microelectrode was then alternately immersed in an ethanol solution of $FeCl_3$ (10 mM) and pyridine (10 mM), deionized water, an aqueous solution of $K_4Fe(CN)_6$ (10 mM) and pyridine (10 mM), and deionized water. These steps were defined as one cycle of layer-

Final edited form was published in "Nano Energy". 2019, 60, S. 8 – 16. ISSN 2211-2855.
https://doi.org/10.1039/C8CC01993B

by-layer (LbL) procedure. By repeating this LbL process for 30, 90, and 150 cycles, a series of thin film samples were grown on the gold substrate (donated as PBpy-*n*L, *n*=30, 90, 150). During the above procedure, the color of gold progressively deepened (Fig. S1), suggesting that the Fe^{3+} ions were initially bounded to 4-mercaptopyridine units, and then complexed with $[Fe(CN)_6]^{4+}$ step-by-step. Meanwhile, pyridine units were expected to preferentially occupy the exposed $[Fe(CN)_6]$ vacancies through direct coordination with Fe(III) rather than H_2O molecules due to the stronger Lewis basicity of the former one [44]. More details can be found in the experimental section. To create a control sample, pure Prussian-blue film (denoted as PB-90L) was prepared by a 90-cycles LbL procedure without the addition of pyridine (Fig. S2). Some complicated post-treatments to obtain the interdigital patterns of thin films can be avoided in above *in-situ* growth method, indicating the scalability and sustainability of this fabrication technology.

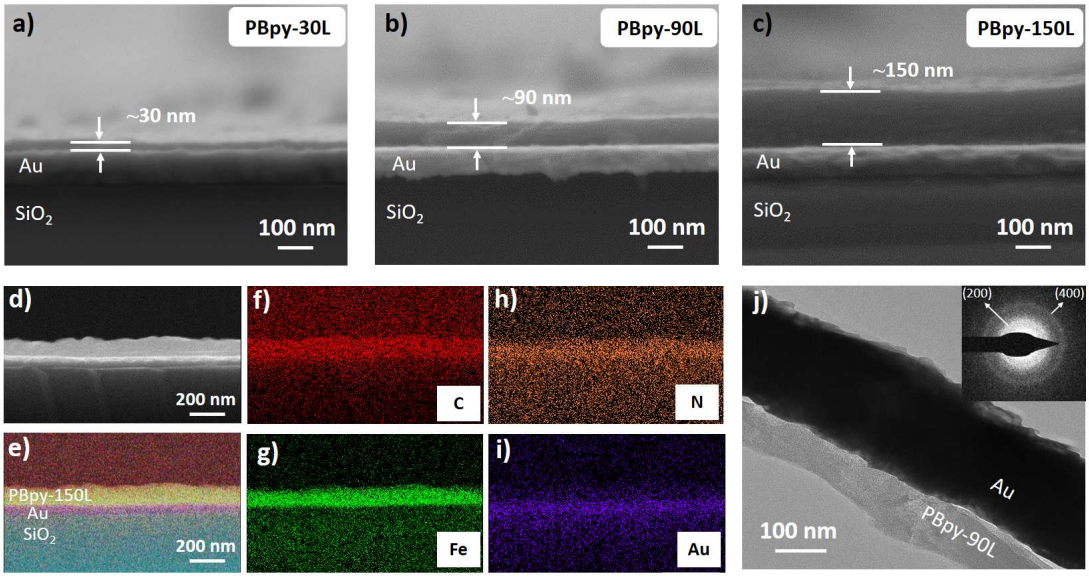

Fig. 2. The morphology characterization of the PBpy-*n*L, including cross-section SEM images of (a) PBpy-30L, (b) PBpy-90L, and (c) PBpy-150L, (d-i) EDS elemental mapping for the cross-section of PBpy-150L, and (j) TEM image for the cross-section of PBpy-90L (inset shows the corresponding SAED pattern).

Final edited form was published in "Nano Energy". 2019, 60, S. 8 – 16. ISSN 2211-2855.
https://doi.org/10.1039/C8CC01993B

The morphologies of the PBpy-*n*L thin films were characterized by scanning electron microscopy (SEM) and transmission electron microscopy (TEM). As displayed in the cross-section SEM images of PBpy-*n*L (Fig. 2a-c), the average thicknesses of PBpy-30L, PBpy-90L, and PBpy-150L were ~30 nm, ~90 nm, and ~150 nm, respectively, indicating that the thicknesses of these thin films could be finely controlled at nanoscale level through the number of cycles in the LbL process. The top-view SEM images of PBpy-*n*L (Fig. S3) manifested uniform and continuous characters. By contrast, the film sample without pyridine modification (i.e. PB-90L, average thickness of ~90 nm), exhibited some distinct cracks in its top-view SEM image (Fig. S4), revealing its relatively poor quality. This phenomenon clearly demonstrated that the presence of pyridine considerably improved the film formation capability of Prussian-blue, probably owing to the vacancy modification at grain boundaries [45]. Furthermore, the energy dispersive X-ray spectroscopy (EDS) elemental mapping for the cross-section of PBpy-150L confirmed that carbon, nitrogen, and iron were uniformly distributed over the thin films (Fig. 2d-i, S5). In the TEM image for the cross-section of PBpy-90L, two diffraction rings in the corresponding selected area electron diffraction (SAED) pattern were evident (inset of Fig. 2j), from which the *d* spaces were measured to be 0.51 and 0.25 nm. These diffraction rings are typically ascribable to the (200) and (400) diffractions of Prussian-blue, respectively [46], indicating that the PBpy thin film featured the intrinsic Prussian-blue structure.

Final edited form was published in "Nano Energy". 2019, 60, S. 8 – 16. ISSN 2211-2855.
https://doi.org/10.1039/C8CC01993B

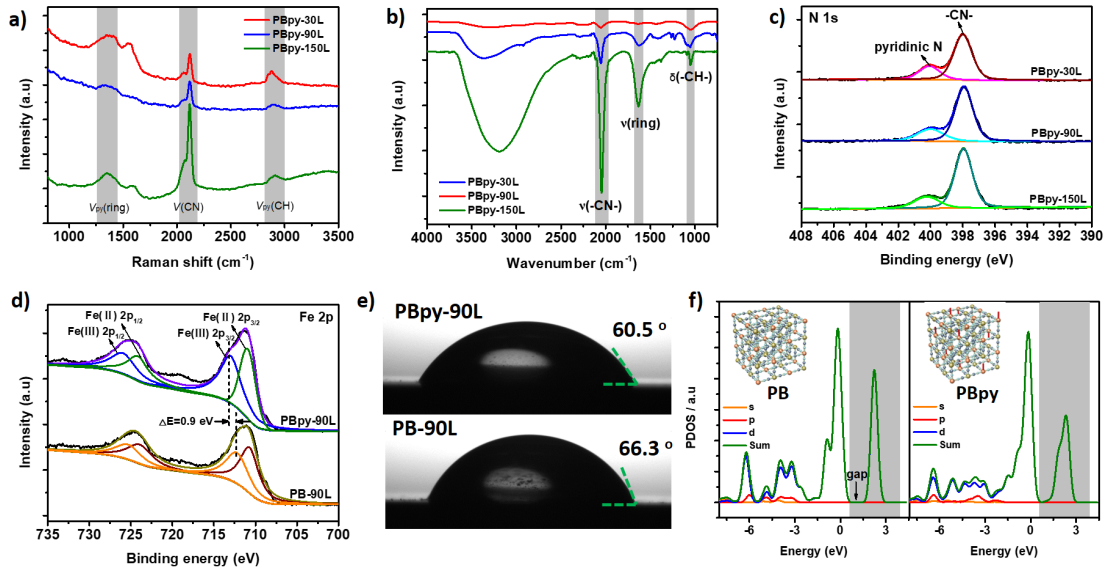

Fig. 3. (a) Raman spectra, (b) IRRAS spectra, and (c) XPS N 1s spectra for the PBpy-*n*L (*n*=30, 90, 150). (d) XPS Fe 2p spectra of PBpy-90L and PB-90L, (e) the water droplet contact angle measurements on PBpy-90L and PB-90L, and (f) the partial density of states (PDOS) of Fe (III) atoms in PBpy and PB.

Further characterizations involving grazing incidence X-ray diffraction (GIXRD) Raman, infrared reflection absorption spectroscopy (IRRAS), and X-ray photoelectron spectroscopy (XPS), thermogravimetric (TG) analysis, inductively coupled plasma atomic emission spectroscopy (ICP-AES), and element analysis were conducted to explore the chemical structural information. Two wide peaks in the GIXRD patterns of PBpy-*n*L (n=30, 90, 150) and PB-90L (Fig. S6) corresponded to the (200) and (400) crystal face of standard Prussian-blue, respectively. The relatively low crystallinity of as-prepared PBpy and PB thin films, which is caused by the LbL synthesis method, can facilitate the exposure of their active sites [47,48]. In the Raman spectra of PBpy-30L, PBpy-90L, and PBpy-150L (Fig. 3a), broad peaks centered at 1354 cm^{-1}, 1353 cm^{-1}, and 1353 cm^{-1}, respectively, were attributed to the stretching vibration of the aromatic ring in pyridine [49]. Moreover, other broad peaks centered at about 2883 cm^{-1}, 2886 cm^{-1}, and

Final edited form was published in "Nano Energy". 2019, 60, S. 8 – 16. ISSN 2211-2855.
https://doi.org/10.1039/C8CC01993B

2889 cm^{-1} for PBpy-30L, PBpy-90L, and PBpy-150L, respectively, can be ascribed to -CH- of pyridine. Besides, the stretching vibration of cyano-group (*v*(-CN-)) was observed located at 2123 cm^{-1} for PBpy-30L, 2119 cm^{-1} for PBpy-90L, and 2118 cm^{-1} for PBpy-150L, respectively. As for the Raman spectrum of PB-90L, only a *v*(-CN-) peak was observed (Fig. S7). In the IRRAS spectra, the *v*(-CN-) peak of PBpy-*n*L (located at about 2045 cm^{-1}, Fig. 3b) exhibited a shift of about 17 cm^{-1} to the low energy regions by comparison with that of PB-90L (2062 cm^{-1}, Fig. S8). This shift was possibly caused by the variation of valence shell orbital energy level of Fe(III) upon the coordination with pyridine [35]. Meanwhile, the broad peaks centered at about 3250-3500 cm^{-1} resulted from the *v*(-OH-) of coordinated water in PBpy-*n*L. In the XPS N 1s spectra, only one peak (397.8 eV) ascribed to the N from -CN- was observed for PB-90L (Fig. S9), and two peaks located at about 399.9 eV and 397.8 eV for PBpy-*n*L (Fig. 3c) were attributed to N from pyridine and -CN-, respectively [50]. Furthermore, the Fe(III) $2p_{3/2}$ peak (713.2 eV) in the XPS Fe 2p spectra of PBpy-*n*L was obviously shifted to the higher energy region over that of PB-90L (712.3 eV), which directly indicated the coordination of strong-field pyridine with Fe(III) (Fig. 3d, S10) [51]. TG analysis (Fig. S11) revealed the mass losses at 250 □ (associated with their water contents [39]) of PBpy-30L, PBpy-90L, PBpy-150L, and PB-90L were 14.3 %, 15.3%, 16.2%, and 20.9%, respectively, verifying the water contents of PBpy-*n*L (n=30, 90, 150) were less than that of PB-90L. Meanwhile, ICP-AES and elemental analysis were conducted to acquire the element contents of PBpy-*n*L (n=30, 90, 150) and PB-90L (Table S1). Based on these results, the vacancy contents of PBpy-*n*L were obtained as about 8%, while that of PB-90L was about 17%.

Final edited form was published in "Nano Energy". 2019, 60, S. 8 – 16. ISSN 2211-2855.
https://doi.org/10.1039/C8CC01993B

These results demonstrated the vacancies within the PBpy framework were largely occupied by pyridine units instead of H_2O.

The surface wetting capability of the PBpy thin film was examined through water droplet contact angle measurements. Notably, the contact angles for PB-90L film (66.3^o) was larger than that for PBpy-90L film (60.5^o), demonstrating that the latter one exhibited better hydrophilicity (Fig. 3e), which might be attributed to the changed surface polarity of PBpy-90L films as the rigid planar pyridine units became part of the channels [45]. Besides, the contact angles of PBpy-30L and PBpy-150L were 62.9^o and 52.3^o, respectively (Fig. S12). The improved hydrophilicity is helpful for the mass transport and electron transfer between hydrogel-electrolyte and the PBpy-based electrode. Moreover, density functional theory (DFT) calculations were performed to determine the difference in the partial density of states (PDOS) of Fe(III) atoms before and after the incorporation of pyridine units (Fig. 3f). The peak width of the PDOS above the Fermi level for Fe(III) atoms in PBpy turned to be broader than those in PB, which indicated the occurrence of electron delocalization around Fe(III) center atoms upon the coordination with pyridine. This electron delocalization is favorable for enhancing their electrochemical activity [52,53]. Obviously, this first report of precise modification at the central metal atoms within the Prussian-blue network may be an effective tool for declining the conventional vacancy-induced suppression of electrochemical activity.

Final edited form was published in "Nano Energy". 2019, 60, S. 8 – 16. ISSN 2211-2855.
https://doi.org/10.1039/C8CC01993B

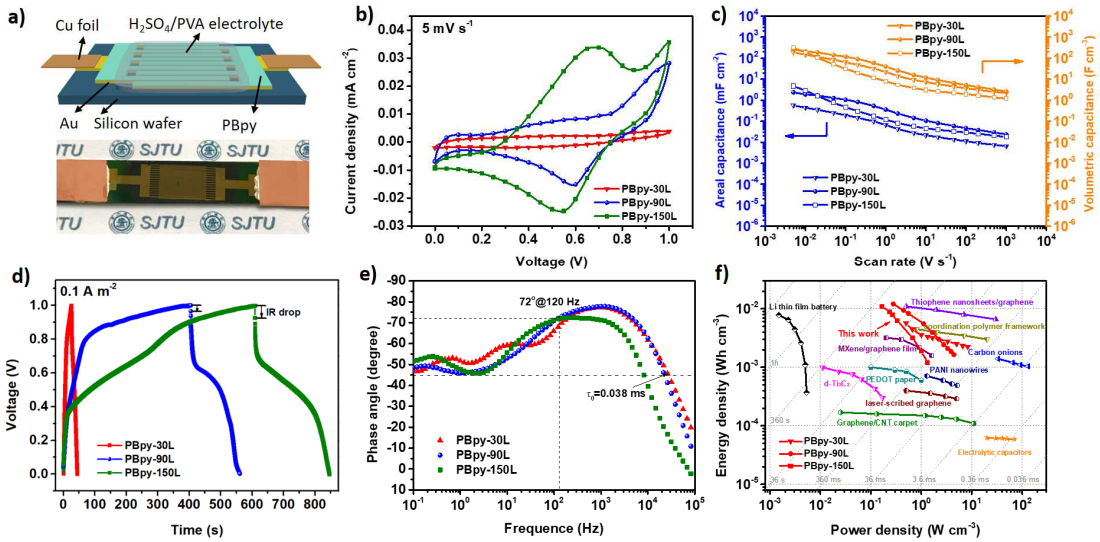

Fig. 4. (a) Schematic diagram and optical image of the PBpy-*n*L-MSCs. The electrochemical performance of the PBpy-*n*L-MSCs, involving (b) CV curves at a scan rate of 5 mV s^{-1}, (c) the specific areal and volumetric capacitances (C_A and C_V) at different scan rate, (d) GCD curves at a current density of 0.1 A m^{-2}, (e) the impedance phase angle at different frequencies, and (f) Ragone plot compared with some previous reported electrochemical energy storage devices including Li thin film battery [18], electrolytic capacitors [9], and MSCs based on graphene/CNT carpet [61], laser-scribed graphene [11], carbon-onions [18], thiophene nanosheets/graphene [60], MXene/graphene film [58], d-Ti_3C_2 [62], PEDOT paper [55], PANI nanowires [28], and azulene-bridged coordination polymer framework [35].

Although Prussian-blue has a high density of redox active site, it has not been explored for the fabrication of MSCs. The resultant PBpy-*n*L films were then investigated as electrodes for the MSCs devices (denoted as PBpy-*n*L-MSCs, n=30, 90, 150), using gel H_2SO_4/PVA (polyvinyl alcohol) as the electrolyte (Fig. 4a). Their electrochemical behaviors were first evaluated through cyclic voltammetry (CV) measurement at the scan rates of 5 mV s^{-1} to 1000 V s^{-1}. The CV curves at the scan rate of 5 mV s^{-1} for PBpy-*n*L-MSCs (Fig. 4b) showed the obvious pseudo-capacitance character, attributable to the H^+ insertion/extraction within the Prussian-blue network through the following reaction: $Fe^{III}_4[Fe^{II}(CN)_6]_3+4H^++4e^-=H_4Fe^{II}_4[Fe^{II}(CN)_6]_3$ [36]. Based on the CV curves, the specific areal and volumetric capacitances (C_A and C_V) for PBpy-*n*L-MSCs at 5 mV s^{-1}

Final edited form was published in "Nano Energy". 2019, 60, S. 8 – 16. ISSN 2211-2855.
https://doi.org/10.1039/C8CC01993B

were calculated as: PBpy-30L-MSC (0.57 mF cm^{-2} and 188 F cm^{-3}), PBpy-90L-MSC (2.38 mF cm^{-2} and 264 F cm^{-3}) and PBpy-150L-MSC (4.69 mF cm^{-2} and 312 F cm^{-3}) (Fig. 4c). Nevertheless, PB-90L-MSCs exhibited lower areal and volumetric capacitances (C_A=1.34 mF cm^{-2} and C_V=150 F cm^{-3}) (Fig. S13) than PBpy-90L-MSC, revealing that the pyridine units within the PBpy film efficiently promote the capacitive performance of the MSC device. Furthermore, the C_V of the fabricated PBpy-*n*L-MSCs are much higher than those of most other reported in-plane MSCs based on different electrode materials, such as vertically aligned rGO (171 F cm^{-3}) [54], PEDOT paper (144 F cm^{-3}) [55], exfoliated graphene/V_2O_5 (131 F cm^{-3}) [56], PANI nanowires (105 F cm^{-3}) [28], MoS_2-rGO/CNT (5.2 F cm^{-3}) [57], MXene/graphene film (33 F cm^{-3}) [58], and azulene-bridged coordination polymer framework (34.1 F cm^{-3}) [35]. Additionally, the C_V for PBpy-30L-MSC, PBpy-90L-MSC, and PBpy-150L-MSC gradually decreased upon the increasing scan rates, for example, with capacitances remained at 4.9, 6.3, and 2.2 F cm^{-3} at 100 V s^{-1} (Fig. S14a), respectively, unveiling their good rate capability.

To further explore the capacitive performance of the PBpy-*n*L-MSCs, galvanostatic charge/discharge (GCD) curves (Fig. 4d) were measured. The internal resistance (IR) drop in the GCD curve reflects the conductivity and internal resistance of electrode materials [56]. Almost no IR drop for PBpy-30L-MSCs revealed that PBpy-30L possessed the highest conductivity and lowest internal resistance of PBpy-*n*L. On the basis of GCD curves, the C_V for PBpy-30L-MSC, PBpy-90L-MSC, and PBpy-150L-MSC (Fig. S14b) were 121, 347 and 318 F cm^{-3}, respectively. It has been demonstrated that the thicker coordination polymer-based thin film offered the higher potential barrier height for ions penetration [29]. Accordingly, the thinnest PBpy-30L exhibited the

Final edited form was published in "Nano Energy". 2019, 60, S. 8 – 16. ISSN 2211-2855.
https://doi.org/10.1039/C8CC01993B

weakest hindrance of ions insertion and diffusion and thus possessed better conductivity, lower internal resistance, and higher rate capability as an electrode for MSC than PBpy-90L and PBpy-150L. Benefiting from both capacitance and rate capability, an active layer with a thickness of ~90 nm in the case of PBpy-90L-MSC exhibited the highest C_V among PBpy-*n*L-MSCs at a current density of 0.1 A m^{-2}. Therefore, an appropriate thickness of PBpy thin films is necessary to achieve high electrochemical performance, revealing finely controlling the thickness of coordination polymer-based thin films is essential for their further application in energy storage fields.

Electrochemical impedance spectroscopy (EIS) measurement was performed to further evaluate the capacitive performance of the PBpy-*n*L-MSCs. The Nyquist plot in high-frequency region for PBpy-90L-MSC showed the lowest equivalent series resistance (ESR) of 5.9 Ω among the PBpy-*n*L-MSCs (Fig. S15a, b), which was calculated from the intercept of the real axis, implying its fast ion transport at electrode-electrolyte interface. The equivalent circuit fitting of these Nyquist plots revealed the charge transfer resistances (R_{ct}) of PBpy-30L-MSC, PBpy-90L-MSC, and PBpy-150L-MSC (Fig. S15c, d) were 0.1, 8.2, and 158.0 Ω, respectively, indicating the best conductivity of PBpy-30L. Furthermore, the phase angle at 120 Hz of PBpy-90L-MSC reached 72^o, which was higher than that of PB-90L-MSC (57^o) (Fig. 4e, S16). It suggested PBpy-90L-MSC was closer to an ideal-capacitor (with a phase angle of 90^o at 120 Hz) [59] than PB-90L. Moreover, the characteristic frequencies (f_0) at a phase angle of -45° for PBpy-30L-MSC, PBpy-90L-MSC, and PBpy-150L-MSC were 26120, 21530, and 8252 Hz, respectively. The corresponding RC time constants τ_0 ($\tau_0=1/f_0$), which indicated the time required for discharging 63.2% of the energy from the entire device [11], were 0.038, 0.046, and

Final edited form was published in "Nano Energy". 2019, 60, S. 8 – 16. ISSN 2211-2855.
https://doi.org/10.1039/C8CC01993B

0.120 ms for PBpy-30L-MSC, PBpy-90L-MSC, and PBpy-150L-MSC, respectively. Importantly, the τ_0 values achieved for the PBpy-*n*L-MSCs were quite lower than those of the reported in-plane MSCs with various electrode materials, such as onion-like carbon (26 ms) [18], laser-scribed graphene (19 ms) [11], 3D graphene/CNT (0.74 ms) [59], thiophene nanosheets/graphene film (1.2 ms) [60], and azulene-bridged coordination polymer framework (0.23 ms) [35] (Table S2). To the best of our knowledge, the τ_0 of PBpy-30L-MSC is the best value of the reported MSCs to date. While, the time constant τ_0 of PB-90L-MSC was 0.12 ms (Fig. S16), which was quite higher than that of PBpy-90L-MSC, strongly suggesting that PBpy film possesses a superior capability for instantaneous delivering ultrahigh energy than pure PB film.

The overall performance of the PBpy-*n*L-MSCs was evaluated via Ragone plot with the volumetric energy density and volumetric power density of an entire device (Fig. 4f). PBpy-30L-MSC, PBpy-90L-MSC, and PBpy-150L-MSC delivered energy densities of up to 5.7 mWh cm^{-3} at 0.5 W cm^{-3}, 12.1 mWh cm^{-3} at 0.28 W cm^{-3}, and 11.1 mWh cm^{-3} at 0.17 W cm^{-3} respectively. The PBpy-*n*L-MSCs showed obvious superiority in consideration of energy density, which was one to two orders higher than those of the reported MSCs based on other electrode materials, *e.g.* graphene/CNT carpet (0.2 mWh cm^{-3}) [61], MXene/graphene film (3.2 mWh cm^{-3}) [58], d-Ti_3C_2 (1.1 mWh cm^{-3}) [62], PANI nanowires (0.7 mWh cm^{-3}) [28], and azulene-bridged coordination polymer framework (4.7 mWh cm^{-3}) [35], and even marginally higher than that of lithium thin-film batteries (7.9 mWh cm^{-3}) [18]. In addition, PBpy-90L-MSC exhibited notable cycling stability with 85% capacitance maintained after 1000 charge/discharge cycles (Fig. S17), which was much better than our previous coordination polymer-based MSC

Final edited form was published in "Nano Energy". 2019, 60, S. 8 – 16. ISSN 2211-2855.
https://doi.org/10.1039/C8CC01993B

[35]. The slight capacitive performance degradation of PBpy-90L-MSC can be attributed to the collapse of crystal framework caused by the repeating insertion/extraction of external ions [41].

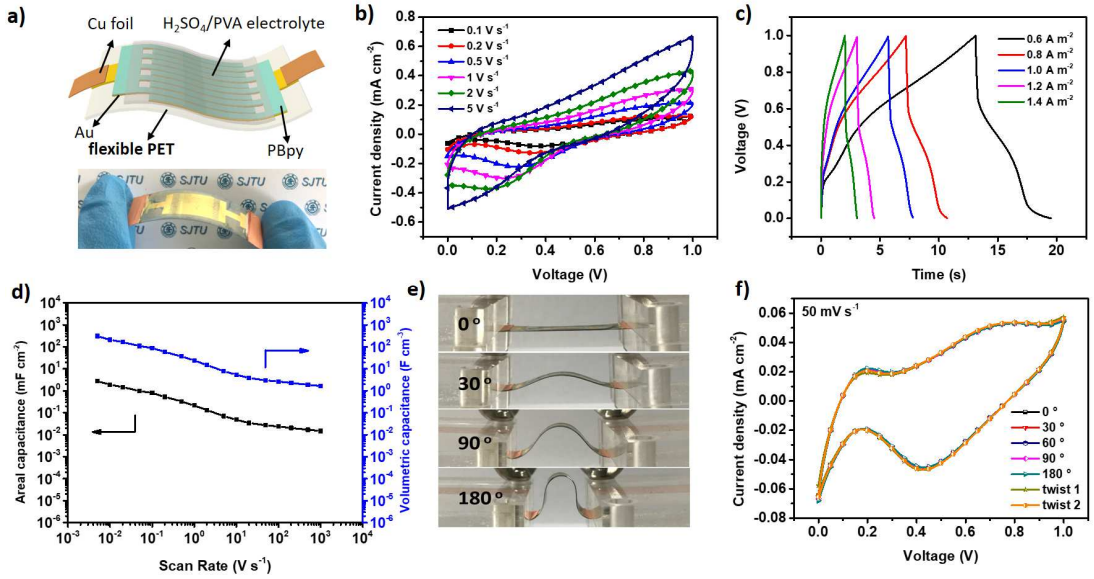

Fig. 5. (a) Schematic diagram and optical image for flexible PBpy-based MSC (donated as *f*-PBpy-90L-MSC) using PET film as substrate. The electrochemical performance of *f*-PBpy-90L-MSC including (b) CV curves at different scan rates, (c) GCD curves at different current densities, and (d) the specific areal and volumetric capacitances (C_A and C_V) calculated from CV curves. (e) Optical images of *f*-PBpy-90L-MSC under different bending conditions, and (f) CV curves for *f*-PBpy-90L-MSC at a scan rate of 50 mV s^{-1} under different bending or twisting conditions.

We further fabricated flexible MSC device (denoted as *f*-PBpy-90L-MSC) with polyethylene terephthalate (PET) film as substrate by using the same LbL procedure for 90 cycles (Fig. 5a). According to the CV curves and GCD curves (Fig. 5b, c, S18), the C_A and C_V of *f*-PBpy-90L-MSC (Fig. 5d) reached up to 2.77 mF cm^{-2} and 308 F cm^{-3}, with the time constant τ_0 of 0.026 ms (Fig. S19a). The Ragone plot disclosed that *f*-PBpy-90L-MSC delivered a remarkable specific energy density of up to 15 mWh cm^{-3} at 0.55 W cm^{-3} (Fig. S19b). Moreover, *f*-PBpy-90L-MSC exhibited the well-maintained CV behavior under the different bending angles of 0^o, 30^o, 60^o, 90^o, 180^o and even twisting states (Fig.

Final edited form was published in "Nano Energy". 2019, 60, S. 8 – 16. ISSN 2211-2855.
https://doi.org/10.1039/C8CC01993B

5e, f, S20, 21), suggesting that MSCs based on PBpy thin film possessed robust mechanical flexibility, which can be potentially useful for the portable and wearable electronics.

3. Conclusion

In summary, the precise modification of $[Fe(CN)_6]$ vacancies within the Prussian-blue network via coordination of pyridine units into Fe(III) was firstly achieved using an *in-situ* growth method. It resulted in the formation of PBpy thin films with finely tuned nanoscale thicknesses *in-situ* grown on the gold interdigital current collectors which can directly serve as electrodes for MSCs. Confirmed by experimental results and density functional theory calculation, the precise vacancy modification within Prussian-blue network improved the film-forming property, hydrophilicity, and electrochemical activity of the thin films. The resultant PBpy-based MSCs exhibited promising electrochemical performance, offering areal and volumetric capacitances of up to 4.77 mF cm^{-2} and 347 F cm^{-3}, respectively, as well as the superior volumetric energy densities of up to 12.1 mWh cm^{-3}. The achieved ultra-low RC time constant (τ_0) of 0.038 ms for PBpy-based MSCs was the best value of the state-of-the-art in-plane MSCs. It is also manifested that a suitable thickness of PBpy thin film is necessary to fabricate high-performance MSCs. Moreover, PBpy-based MSCs with remarkable mechanical flexibility are highly desirable for portable and wearable appliances. Our work provides an attractive solution for structural engineering of promising active materials on molecule level toward high-performance micro-energy devices.

Final edited form was published in "Nano Energy". 2019, 60, S. 8 – 16. ISSN 2211-2855.
https://doi.org/10.1039/C8CC01993B

4. Experimental section

Materials: All the reagents and solvents, including $FeCl_3 \cdot 6H_2O$, $K_4Fe(CN)_6 \cdot 3H_2O$, pyridine (GC, 99.9%), and ethanol (GC, 99.8%), were purchased from commercial suppliers such as Sigma-Aldrich and Adamas-beta. All the available chemicals were used without further purification.

Fabrication of microelectrode: Interdigital Au microelectrodes were prepared through thermal evaporation of Au using a lab-made mask. SiO_2/silicon wafer (single side polished, 500 nm SiO_2 layer) was used as substrate. A removable mask with 30 interdigital-fingers (width of 200 μm, interspace of 80 μm) was fixed onto the silicon wafer, followed by the evaporation of Au with a rate of 1.0 Å s^{-1} and chamber pressure at ~2.0×10^{-6} Torr. As for flexible microelectrode, commercial polyethylene terephthalate (PET) film (thickness of 100 μm) was used as substrate with the same above processing.

Fabrication of PBpy thin films: PBpy thin films were prepared by an *in-situ* growth method, resulting in the direct formation of PBpy thin film on Au interdigital microelectrode that was patterned on SiO_2/silicon wafer or PET substrates. Typically, Au-microelectrode on silicon wafer was firstly immersed in an ethanol solution of 4-mercaptopyridine (2 mM) for 12 hours, resulting in the functionalization of Au. Subsequently, the Au-microelectrode was washed with fresh ethanol for 3 times to remove the uncoordinating 4-mercaptopyridine. Next, the functionalized microelectrode was immersed in an ethanol solution of $FeCl_3$ (10 mM) and pyridine (10 mM) for 30 s, with subsequently being soaked in a deionized water for 15 s to remove unreacted reagents. Then, the microelectrode was immersed in another aqueous solution of $K_4Fe(CN)_6$ (10 mM) and pyridine (10 mM) for 30 s, followed by being soaked in the deionized water for 15 s. The above four immersing steps were considered as one cycle. By repeating such LbL procedures for 30 cycles, 90 cycles, and 150 cycles, the thin films donated as PBpy-30L, PBpy-90L, and PBpy-150L were obtained, respectively.

A control sample of pure Prussian-blue thin film (PB-90L) was prepared through the same procedure as PBpy-90L without the addition of pyridine during the LbL process.

The flexible MSC based on PBpy thin film (signed as *f*-PBpy-90L MSC) was also prepared by the LbL procedures of alternately soaking the as-prepared flexible microelectrode on PET film, which was functionalized by 4-mercaptopyridine as well, in

Final edited form was published in "Nano Energy". 2019, 60, S. 8 – 16. ISSN 2211-2855.
https://doi.org/10.1039/C8CC01993B

an ethanol solution of $FeCl_3$ (10 mM) and pyridine (10 mM), a deionized water, an aqueous solution of $K_4Fe(CN)_6$ (10 mM) and pyridine (10 mM), and a deionized water for 90 cycles.

Materials characterization: Scanning Electron Microscopy (SEM) measurements and corresponding energy dispersive X-ray spectroscopy (EDS) elemental mapping were performed on JEOL JSM-7800F Prime field emission scanning electron microscope. Transmission electron microscopy (TEM) measurements and corresponding selected area electron diffraction (SAED) pattern were performed by Talos F200X field emission transmission electron microscope from FEI, and the sample was prepared by Cryo ultramicrotome (UC6-FC6). Raman spectra were obtained by dispersive Raman microscope (Senterra R200-L) with excitation laser wavelength of 532 nm. Infrared reflection absorption spectroscopy (IRRAS) was collected by Spectrum 100 spectrometer (Perkin Elmer, Inc., USA). X-ray photoelectron spectroscopy (XPS) measurements were performed by AXIS Ultra DLD system from Kratos with Al Kα radiation as X-ray source (1486.6 eV), anode voltage/current of 15 kV/10 mA, and neutralizer parameter of 1.6/2.8/1. Grazing incidence X-ray diffraction (GIXRD) measurements were carried out by D8 ADVANCE Da Vinci poly-functional X-ray diffractometer with Cu Kα radiation (wavelength of 1.5418 Å) and grazing incidence angle of 3°. Thermogravimetric (TG) analysis was measured using a Perkin-Elmer Pyris 1 thermo gravimetric analyzer in flowing (100 mL min^{-1}) nitrogen atmosphere with a heating rate of 10 □ min^{-1}. The Fe contents of samples were examined by ICP-AES (iCAP7600). The C and N contents of samples were obtained by elemental analysis (Vario EL Cube). Contact angle measurements were obtained by DSA30 Kruss contact angle measuring device using drop shape method (water droplet).

Electrochemical characterization: Electrolyte of H_2SO_4/PVA gel (1.2 g H_2SO_4 and 6 g PVA mixed with 60 mL deionized water) was dropped on the PBpy thin film carefully and solidified overnight before electrochemical measurements. Besides, Cu foil was adhered on the end of microelectrode by silver paste as connector during electrochemical measurements.

All the electrochemical measurements were conducted using CHI650D electrochemical work-station. Cyclic voltammetry (CV) curves were examined at

Final edited form was published in "Nano Energy". 2019, 60, S. 8 – 16. ISSN 2211-2855.
https://doi.org/10.1039/C8CC01993B

different scan rates from 0.005 to 1000 V s^{-1}. Galvanostatic charge/discharge (GCD) curves were obtained at different current density with voltage window of 0-1 V. Electrochemical impedance spectroscopy (EIS) was performed at the frequency ranging from 0.01 to 100000 Hz with 5 mV AC amplitude.

Electrochemical calculations: The electrode specific capacitance values can be calculated from CV curves according to the following equation (1) and (2):

$$C_A = \frac{1}{v \times A \times (V_f - V_i)} \int_{V_i}^{V_f} I(V) dV \quad (1)$$

$$C_V = \frac{1}{v \times V \times (V_f - V_i)} \int_{V_i}^{V_f} I(V) dV \quad (2)$$

where C_A is donated as specific areal capacitance (mF cm^{-2}) of PBpy-based MSC, v is the scan rate (V s^{-1}), V_f and V_i are the integration potential limits of the voltammetric curve, and $I(V)$ is the voltammetric CV current (A), A (cm^{-2}) is the area of single electrode, which is 0.3 cm^{-2} for all the resultant MSCs. C_V is donated as specific volume capacitance (F cm^{-3}) of PBpy-based MSC and V (cm^{-3}) is the volume of single electrode, which is 0.9×10^{-8} cm^{-3} for PBpy-30L-MSC, 2.7×10^{-8} cm^{-3} for PBpy-90L-MSC, PB-90L-MSC or *f*-PBpy-90L-MSC, and 4.5×10^{-8} cm^{-3} for PBpy-150L-MSC.

The specific areal capacitance (C_A, mF cm^{-2}) and specific volume capacitance (C_V, F cm^{-3}) were calculated from GCD curves as well according to the following equation (3) and (4):

$$C_A = \frac{J \times \Delta t}{\Delta V} \quad (3)$$

$$C_V = \frac{C_A}{d} \quad (4)$$

where J is the current density (A m^{-2}) of charge/discharge, Δt is the discharged time (s), ΔV is discharge voltage range (V), and d is the thickness of PBpy-*n*L (30 nm for PBpy-30L, 90 nm for PBpy-90L or PB-90L, and 150 nm for PBpy-50L).

The volume energy density (E, Wh cm^{-3}) and volume power density (P, W cm^{-3}) of the whole device in the Ragone plot were calculated from GCD curves referred the equations (5) and (6) as follows:

$$E = \frac{1}{2} \times \frac{C_V}{4} \times \frac{(\Delta V)^2}{3600} \quad (5)$$

$$= \frac{E}{\Delta t} \times 3600 \quad (6)$$

Final edited form was published in "Nano Energy". 2019, 60, S. 8 – 16. ISSN 2211-2855.
https://doi.org/10.1039/C8CC01993B

where C_V is specific volume capacitance of PBpy-based MSC, ΔV is discharge voltage range (V), and Δt is the discharged time (s).

Calculation method: Density functional theory (DFT) simulations based on the first principles calculations in the framework of density functional theory, including structural, electronic performances, were carried out by the Cambridge Sequential Total Energy Package known as CASTEP. The exchange-correlation functional under the generalized gradient approximation (GGA) with norm-conserving pseudopotentials and Perdew-Burke-Ernzerhof functional was adopted to describe the electron-electron interaction. An energy cutoff of 750 eV was used and a k-point sampling set of 5×5×1 was tested to be converged. A force tolerance of 0.01 eV $Å^{-1}$, energy tolerance of 5.0×10^{-7} eV per atom and maximum displacement of 5.0×10^{-4} Å were considered. Each atom in the storage models is allowed to relax to the minimum in the enthalpy without any constraints. The vacuum space along the z-direction is set to be 15 Å, which is enough to avoid interaction between the two neighboring images.

Acknowledgements

This work was financially supported by Shanghai Committee of Science and Technology (16JC1400703, 15JC1490500); National Natural Science Foundation of China for Excellent Young Scholars (51722304); NSFC (21574080, 21774072, 21720102002), Open Project Programs of the State Key Laboratory of Inorganic Synthesis and Preparative Chemistry (2019-01, Jinli University State Key), Laboratory of Supramolecular Structure and Materials (sklssm201732, Jilin University); German Research Foundation (DFG) within the Cluster of Excellence "Center for Advancing Electronics Dresden" (cfaed), EU Graphene Flagship. P. Zhang thanks the financial support from the Initiative and Networking Fund of the German Helmholtz Association, Helmholtz International Research School for Nanoelectronic Networks NanoNet (VH-KO-606). Y. He thanks the China Scholarship Council (CSC).

References

[1] Y. Shao, M. F. El-Kady, L. J. Wang, Q. Zhang, Y. Li, H.Wang, M. F. Mousavi, R. B. Kaner, Chem. Soc. Rev. 44 (2015) 3639-3665.
[2] P. Zhang, F. Wang, M. Yu, X. Zhuang, X. Feng, Chem. Soc. Rev. 47 (2018) 7426-7451.
[3] M. Beidaghi, Y. Gogotsi, Energy Environ. Sci. 7 (2014) 867-884.
[4] D. P. Dubal, N. R. Chodankar, D. H. Kim, P. Gomez-Romero, Chem. Soc. Rev. 47 (2018) 2065-2129.

[5] N. Kurra, Q. Jiang, H. N. Alshareef, Nano Energy 16 (2015), 1-9.
[6] Y. Da, J. Liu, L. Zhou, X. Zhu, X. Chen, L. Fu, Adv. Mater. 30 (2018) 1802793.
[7] D. Qi, Y. Liu, Z. Liu, L. Zhang, X. Chen, Adv. Mater. 29 (2017) 1602802.
[8] J. Chmiola, C. Largeot, P.-L. Taberna, P. Simon, Y. Gogotsi, Science 328 (2010) 480-483.
[9] M. F. El-Kady, V. Strong, S. Dubin and R. B. Kaner, Science 335 (2012) 1326-1330.
[10] W. Gao, N. Singh, L. Song, Z. Liu, A. L. M. Reddy, L. Ci, R. Vajtai, Q. Zhang, B. Wei, P. M. Ajayan, Nat. Nanotechnol. 6 (2011) 496-500.
[11] M. F. El-Kady, R. B. Kaner, Nat. Commun. 4 (2013) 1475.
[12] X. Shi, S. Pei, F. Zhou, W. Ren, H.-M. Cheng, Z.-S. Wu, X. Bao, Energy Environ. Sci. (2019) DOI: 10.1039/C8EE02924E.
[13] Z.-S. Wu, Z. Liu, K. Parvez, X. Feng, K.Müllen, Adv. Mater. 27 (2015) 3669-3675.
[14] J. Li, S. S. Delekta, P. Zhang, S. Yang, M. R. Lohe, X. Zhuang, X. Feng, M. Östling, ACS Nano 11 (2017) 8249-8256.
[15] K.-H. Choi, J. Yoo, C. K. Lee, S.-Y.Lee, Energy Environ. Sci. 9 (2016) 2812-2821.
[16] H. Pang, Y. Zhang, W.-Y. Lai, Z. Hu, W. Huang, Nano Energy, 15 (2015) 303-312.
[17] Z. Liu, Z.-S. Wu, S. Yang, R. Dong, X. Feng, K. Müllen, Adv. Mater. 28 (2016) 2217-2222.
[18] D. Pech, M. Brunet, H. Durou, P. Huang, V. Mochalin, Y. Gogotsi, P.-L. Taberna, P. Simon, Nat. Nanotechnol. 5 (2010) 651-654.
[19] Z.-S.Wu, Y.-Z. Tan, S. Zheng, S. Wang, K. Parvez, J. Qin, X. Shi, C. Sun, X. Bao, X. Feng, K. Müllen, J. Am. Chem. Soc. 139 (2017) 4506-4512.
[20] G. Lee, D. Kim, D. Kim, S. Oh, J. Yun, J. Kim, S.-S. Lee, J. S. Ha, Energy Environ. Sci. 8 (2015) 1764-1774.
[21] W. Si, C. Yan, Y. Chen, S. Oswald, L. Han, O. G. Schmidt, Energy Environ. Sci. 6 (2013) 3218-3223.
[22] H. Wu, K. Jiang, S. Gu, H. Yang, Z. Lou, D. Chen, G. Shen, Nano Res. 8 (2015) 3544-3552.
[23] J. Wu, J. Peng, Z. Yu, Y. Zhou, Y. Guo, Z. Li, Y. Lin, K. Ruan, C. Wu, Y. Xie, J. Am. Chem. Soc. 140 (2018) 493-498.
[24] Z. Li, M. Shao, L. Zhou, R. Zhang, C. Zhang, J. Han, M. Wei, D. G. Evans, X. Duan, Nano Energy 20 (2016) 294-304.
[25] N. Kurra, B. Ahmed, Y. Gogotsi, H. N. Alshareef, Adv. Energy Mater. 6 (2016) 1601372
[26] P. Zhang, J. Wang, W. Sheng, F. Wang, J. Zhang, F. Zhu, X. Zhuang, R. Jordan, O. G. Schmidt, X. Feng, Energy Environ. Sci. 11 (2018) 1717-1722.
[27] M. Zhu, Y. Huang, Y. Huang, H. Li, Z. Wang, Z. Pei, Q. Xue, H. Geng, C. Zhi, Adv. Mater. 29 (2017) 1605137.
[28] C. Meng, J. Maeng, S. W. M. John, P. P. Irazoqui, Adv. Energy Mater. 4 (2014) 1301269.
[29] S. Sakaida, K. Otsubo, O. Sakata, C. Song, A. Fujiwara, M. Takata, H. Kitagawa, Nat. Chem. 8 (2016) 377-383.
[30] Stassen, M. Styles, G. Grenci, H. V. Gorp, W. Vanderlinden, S. D. Feyter, P. Falcaro, D. D. Vos, P. Vereecken, R. Ameloot, Nat. Mater. 15 (2016) 304-310.
[31] D. Bradshaw, A. Garai, J. Huo, Chem. Soc. Rev. 41 (2012) 2344-2381.

[32] D. Sheberla, J. C. Bachman, J. S. Elias, C.-J. Sun, Y. Shao-Horn, M. Dinca, Nat. Mater. 16 (2017) 220-224.
[33] D. Feng, T. Lei, M. R. Lukatskaya, J. Park, Z. Huang, M. Lee, L. Shaw, S. Chen, A. A. Yakovenko, A. Kulkarni, J. Xiao, K. Fredrickson, J. B. Tok, X. Zou, Y. Cui, Z. Bao, Nat. Energy 3 (2018) 30-36.
[34] T. Deng, Y. Lu, W. Zhang, M. Sui, X. Shi, D. Wang, W. Zheng, Adv. Energy Mater. 8 (2018) 1702294.
[35] C. Yang, K. S. Schellhammer, F. Ortmann, S. Sun, R. Dong, M. Karakus, Z. Mics, M. Löffler, F. Zhang, X. Zhuang, E. Cánovas, G. Cuniberti, M. Bonn, X. Feng, Angew. Chem. Int. Ed. 56 (2017) 3920-3924.
[36] J. Qian, C. Wu, Y. Cao, Z. Ma, Y. Huang, X. Ai, H. Yang, Adv. Energy Mater. 8 (2018) 1702619.
[37] J.-G. Wang, Z. Zhang, X. Zhang, X. Yin, X. Li, X. Liu, F. Kang, B. Wei, Nano Energy 39 (2017) 647-653.
[38] B. Kong, C. Selomuly, G.Zheng, D. Zhao, Chem. Soc. Rev. 44 (2015) 7997-8018.
[39] M. Pasta, C. D. Wessells, N. Liu, J. Nelson, M. T. McDowell, R. A. Huggins, M. F. Toney, Y. Cui, Nat. Commun. 5 (2014) 3007.
[40] P. R. Bueno, D. Giménez-Romero, C. Gabrielli, J. García-Jareño, H. Perrot, F. Vicente, J. Am. Chem. Soc. 128 (2006) 17146-17152.
[41] Y. You, X.-L. Wu, Y.-X Yin, Y.-G. Guo, Energy Environ. Sci. 7 (2014) 1643-1647.
[42] Y. Jiang, S. Yu, B. Wang, Y. Li, W. Sun, Y. Lu, M. Yan, B. Song, S. Dou, Adv. Funct. Mater. 26 (2016) 5315-5321.
[43] D. Yang, J. Xu, X.-Z. Liao, H. Wang, Y.-S. He, Z.-F. Ma, Chem. Commun. 51 (2015) 8181-8184.
[44] J. S. Seo, D. Whang, H. Lee, S. I. Jun, J. Oh, Y. J. Jeon, K. Kim, Nature 404 (2000) 982-986.
[45] D. Bi, X. Li, J. V. Milić, D. J. Kubicki, N. Pellet, J. Luo, T. LaGrange, P. Mettraux, L. Emsley, S. M. Zakeeruddin, M. Grätzel, Nat. Commun. 9 (2018) 4482.
[46] M. J. Piernas-Muñoz, E. Castillo-Martínez, V. Roddatis, M. Armand, T. Rojo, J. Power Sources 271 (2014) 489-496.
[47] R. D. L. Smith, M. S. Prévot, R. D. Fagan, Z. Zhang, P. A. Sedach, M. K. J. Siu, S. Trudel, C. P. Berlinguette, Science 340 (2013) 60-63.
[48] A. Indra, P. W. Menezes, N. R. Sahraie, A. Bergmann, C. Das, M. Tallarida, D. Schmeißer, P. Strasser, M. Driess, J. Am. Chem. Soc. 136 (2014) 17530-17536.
[49] T. Haraguchi, K. Otsubo, O. Sakata, A. Fujiwara and H. Kitagawa, J. Am. Chem. Soc. 138 (2016) 16787-16793.
[50] Y. Zou, Q. Wang, C. Xiang, Z. She, H. Chu, S. Qiu, F. Xu, S. Liu, C. Tang, L. Sun, Electrochim. Acta 188 (2016) 126-134.
[51] Y. Teng, X.-D. Wang, J.-F. Liao, W.-G. Li, H.-Y. Chen, Y.-J. Dong, D.-B Kuang, Adv. Funct. Mater. 28 (2018) 1802463.
[52] K. Gong, F. Du, Z. Xia, M. Durstock, L. Dai, Science 323 (2009) 760-764.
[53] C. H. Choi, S. H. Park, S. I. Woo, ACS Nano 6 (2012) 7084-7091.
[54] Y. Yoon, K. Lee, S. Kwon, S. Seo, H. Yoo, S. Kim, Y. Shin, Y. Park, D. Kim, J.-Y. Choi, H. Lee, ACS Nano 8 (2014) 4580-4590.
[55] B. Anothumakkool, R. Soni, S. N. Bhange, S. Kurungot, Energy Environ. Sci. 8 (2015) 1339-1347.

[56] P. Zhang, F. Zhu, F. Wang, J. Wang, R. Dong, X. Zhuang, O. G. Schmidt, X. Feng, Adv. Mater. 29 (2017) 1604491.
[57] G. Sun, X. Zhang, R. Lin, J. Yang, H. Zhang, P. Chen, Angew. Chem. Int. Edit. 54 (2015) 4651-4656.
[58] H. Li, Y. Hou, F. Wang, M. R. Lohe, X. Zhuang, L. Niu, X. Feng, Adv. Energy Mater. 7 (2017) 1601847.
[59] J. Lin, C. Zhang, Z. Yan, Y. Zhu, Z. Peng, R. H. Hauge, D. Natelson, J. M. Tour, Nano Lett. 13 (2013) 72-78.
[60] Z.-S. Wu, Y. Zheng, S. Zheng, S. Wang, C. Sun, K. Parvez, T. Ikeda, X. Bao, K. Müllen, X. Feng, Adv. Mater. 29 (2017) 1602960.
[61] M. Beidaghi, C. Wang, Adv. Funct. Mater. 22 (2012) 4501-4510.
[62] M. R. Lukatskaya, O. Mashtalir, C. E. Ren, Y. Dall' Agnese, P. Rozier, P. L. Taberna, M. Naguib, P. Simon, M. W. Barsoum, Y. Gogotsi, Science 341 (2013) 1502-1505.

Yafei He is a PhD candidate at Shanghai Jiao Tong University under the supervision of Prof. Xinliang Feng since September 2015. She received her Bachelor's Degree in 2013 and Master's Degree in 2015 from Harbin Institute of Technology. Between 2017 and 2018, she was a joint PhD student at Technische Universität Dresden (Germany). Her research interests focus on porous polymers and carbon-based porous materials for the applications in energy storage and conversion.

Panpan Zhang received his BS degree in 2012 and MS degree in 2015 from Beijing University of Chemical Technology, China. Currently, he is a PhD candidate under the supervision of Prof. Xinliang Feng in Technische Universität Dresden since July 2015, Germany. His research interests focus on the synthesis of novel two-dimensional materials and their applications in electronics and miniaturized energy storage devices.

Faxing Wang joined Prof. Xinliang Feng's group as a PhD candidate at the Technische Universität Dresden (Germany) in December 2015. He received his Master's Degree in Physical Chemistry in June 2014 at Fudan University. Then he worked as a research assistant in Nanjing Tech University between 2014 and 2015. His current research topics focus on electrochemically energy storage systems based on 2D materials and the related mechanism studies.

Final edited form was published in "Nano Energy". 2019, 60, S. 8 – 16. ISSN 2211-2855.
https://doi.org/10.1039/C8CC01993B

Luxin Wang received his PhD degree from the School of Chemistry and Molecular Engineering, East China University of Science and Technology in 2018. So far he has published several articles in international peer-review journals. His present work is mainly focused on the design and synthesis of electroactive functional materials for polymer devices, including memory and supercapacitor.

Yuezeng Su is currently a professor in School of Electronic Information and Electrical Engineering of Shanghai Jiao Tong University. Prof. Su's research interests focus on functional polymer materials, functional hybrid materials, and carbon-rich materials for electronic and energy-related applications.

Fan Zhang received his BEng degree in electrochemistry from Shanghai Jiao Tong University in 1991, and his Ph.D. in organic chemistry from Jilin University in 2000. After more than 8 years of research experience in Germany and the United States, he was promoted to a Research Professor in School of Chemistry and Chemical Engineering of Shanghai Jiao Tong University, China. His research interests are organic π-conjugated functional materials and porous polymers for energy conversion and storage.

Xiaodong Zhuang is presently a full professor of Shanghai Jiao Tong University in China. His scientific interests include rational designed two dimensional soft materials and carbon-rich porous materials for energy storage and conversion, e.g. metal-air batteries, supercapacitors, and catalytic carbon dioxide reduction reaction, hydrogen evolution reaction, oxygen reduction reaction.

Xinliang Feng is a full professor and has been the head of the Chair of Molecular Functional Materials at Technische Universität Dresden since 2014. He received his BS degree in 2001 and MS degree in 2004. Then he joined Prof. Klaus Müllen's group at the Max Planck Institute for Polymer Research (MPIP), where he obtained his PhD degree in April 2008. In December 2007, he was appointed as a group leader at the MPIP. His current scientific interests include graphene, synthetic two-dimensional materials, organic conjugated materials, and carbon-rich molecules and materials for electronic and energy-related applications.

Final edited form was published in "Nano Energy". 2019, 60, S. 8 – 16. ISSN 2211-2855.
https://doi.org/10.1039/C8CC01993B

Highlights:

1. The first report of precise vacancy modification of Prussian-blue nano-thin films.
2. *In-situ* grown method exhibits the scalability, sustainability, and universality for MSC fabrication.
3. The vacancy modification can improve the film-forming property, hydrophilicity, and electrochemical activity of the thin films.
4. The resultant MSCs exhibit ultrahigh energy densities and ultra-low time constants.
5. This work provides an attractive solution to achieve high performance of new generation miniaturized energy storage devices.